Supplementary Information

Mitigating Redox Mediator-Induced Surface Recombination for Efficient Photoelectrocatalytic Benzyl Alcohol Oxidation on Mo-Doped Bismuth Vanadate

Chun-Chung Kuang,[‡a] Yi-Wen Chen,[‡a] Guan-Zhu Tu,[a] Hong-Lin Chen,[b] Jun-Lin Fong,[a] Yi-Sheng Wang,[a] Chia-Wei Chang,[a] Jing-Yan Wu,[b] Ting-Ting Chang,[a] Chao-Hsien Chang,[a] Hong-Kang Tian,[bcde] Chang-Ming Jiang[*a]*

[a] Department of Chemistry and Center for Emerging Materials and Advanced Devices, National Taiwan University, Taipei 106319, Taiwan

[b] Department of Chemical Engineering, National Cheng Kung University, Tainan 701, Taiwan.

[c] Program on Smart and Sustainable Manufacturing, Academy of Innovative Semiconductor and Sustainable Manufacturing, National Cheng Kung University, Tainan 701, Taiwan

[d] Center for Resilience and Intelligence on Sustainable Energy Research (RiSER), National Cheng Kung University, Tainan 701, Taiwan

[e] Sustainable Electrochemical Energy Development (SEED) Center, National Taiwan University of Science and Technology, Taipei 106, Taiwan

*Corresponding Author: cmjiang@ntu.edu.tw

[‡]These authors contributed equally to this work.

1. Synthesis of Pristine and Mo-doped $BiVO_4$ Photoanodes

Polycrystalline $BiVO_4$ thin films were synthesized on fluorine-doped tin oxide (FTO)-coated glass substrates using a previously reported metal-organic decomposition method.[1] As shown in **Fig. S1**, 0.36 mmol of bismuth (III) nitrate pentahydrate ($Bi(NO_3)_3 \bullet 5H_2O$; >99.9%, Sigma-Aldrich) was dissolved in 0.9 mL of glacial acetic acid (99-100%, Shimakyu), while 0.36 mmol of vanadyl acetylacetonate ($VO(acac)_2$; 98%, Sigma-Aldrich) was dissolved in 6.0 mL of acetylacetone (≥99%, Sigma-Aldrich). After 15 minutes of sonication, a colorless Bi solution and a dark-green V solution were obtained. The two solutions were mixed and sonicated for an additional 30 minutes, resulting in a blue $BiVO_4$ precursor solution, which was then filtered using a 0.2 µm pore size PTFE syringe filter. For Mo-doped $BiVO_4$ films, bis(acetylacetonato)dioxomolybdenum(VI) ($MoO_2(acac)_2$; Sigma-Aldrich) was used to substitute 1% or 3% of $VO(acac)_2$ in the precursor solution.

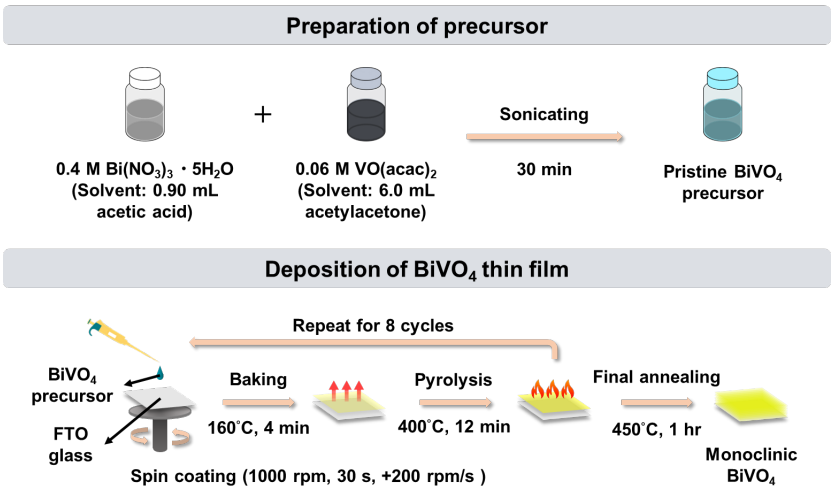

Fig. S1 Schematic diagram of the $BiVO_4$ photoanode synthesis process.

FTO glass substrates (TEC-7, Sigma Aldrich) were cut to 2.5 × 2.5 cm^2 squares and cleaned sequentially in deionized water with detergent, acetone, and isopropyl alcohol using an ultrasonic bath for 15 minutes each. After drying under a nitrogen stream, the FTO glass substrates were treated in a UV-ozone cleaner for 20 minutes. A total of 125 µL of the $BiVO_4$ precursor solution was spin-coated onto each substrate at 1000 rpm for 30 seconds (acceleration: 200 rpm s^{-1}). The as-coated films were heated at 160ºC on a hot plate for 4 minutes, followed by pyrolysis at 400ºC for 12 minutes in a box furnace (CWF 11/05, Carbolite Gero). This spin-coating-baking-pyrolysis cycle was repeated eight times. A final annealing step was performed in air at 450ºC for 1 hour.

2. Characterization of $BiVO_4$ Photoanodes

The elemental composition of Mo-doped $BiVO_4$ films was analyzed by inductively coupled plasma mass spectrometry (ICP-MS, Agilent 7900) following the digestion of the samples in concentrated nitric acid. Quantification was carried out against Bi (0-100 ppb), V (0-100 ppb), and Mo (0-10 ppb) standard solutions (**Table S1**). The positive deviation of the Bi/V ratio from the stoichiometric value is attributed to the vanadium vaporization during the annealing steps. The Mo/(V+Mo) ratios were found to be 1.4% and 3.4% for 1% and 3% Mo:$BiVO_4$ films, close to the substitution ratios in the precursor solutions.

Table S1 Metal compositions of Mo:$BiVO_4$ photoanodes quantified by ICP-MS.

Sample	^{209}Bi (%)	^{51}V (%)	^{95}Mo (%)	Mo/(V+Mo)*100%
1% Mo:$BiVO_4$	53.40	45.95	0.65	1.4%
3% Mo:$BiVO_4$	53.24	45.19	1.57	3.4%

Grazing incidence X-ray diffraction (GIXRD) measurements were performed by a Rigaku SmartLab SE diffractometer equipped with a Cu anode (λ = 1.5406 Å). The X-ray incident angle was fixed at 0.5º, and the 2θ angle was scanned between 20-70º in 0.07º increments. Raman spectra were collected using a UniNano UNIDRON-A spectrometer equipped with a 532 nm excitation laser source.

The sub-µm scale surface morphology of $BiVO_4$ films (**Fig. S2**) was investigated by a field-emission scanning electron microscope (JSM-7600, JEOL) using the secondary electron imaging mode and an acceleration voltage of 10.0 kV. A 1-3 nm thick Pt layer was sputtered onto each film before the microscopic studies.

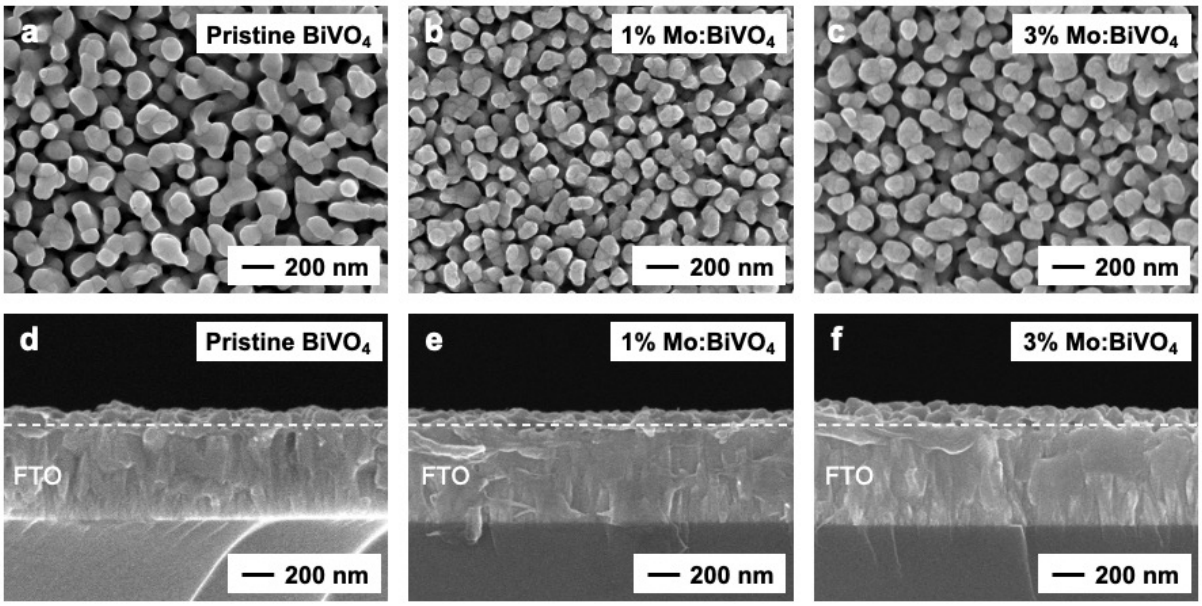

Fig. S2 (a-c) Top-view and (d-f) cross-sectional SEM images of pristine, 1% Mo-doped, and 3% Mo-doped $BiVO_4$ films grown on FTO glass substrate.

The absorption spectra were collected by an ultraviolet-visible (UV-vis) spectrometer (V-770, JASCO) between 400 and 700 nm (**Fig. S3**). Tauc analysis was performed using the formula $(\alpha h\nu)^{1/n} = B(h\nu - E_g)$, in which α represents the absorption coefficient, $h\nu$ the photon energy, B the proportional factor, and E_g the optical bandgap. Here, n is chosen to be 2 to account for the indirectly allowed bandgap of $BiVO_4$, which is situated just 0.2 eV below the direct bandgap.[2]

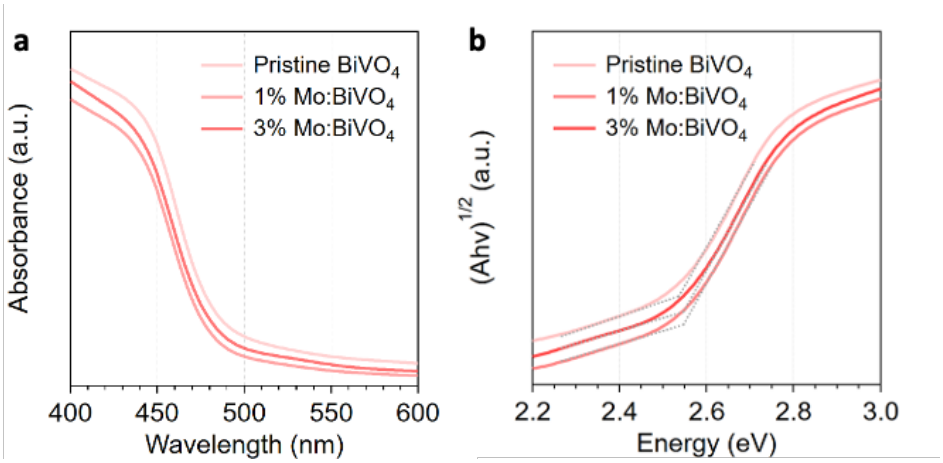

Fig. S3 (a) UV-vis absorption spectra of pristine and Mo-doped $BiVO_4$ films grown on FTO glass substrates. (b) Tauc plots for an indirectly allowed interband transition.

X-ray photoelectron spectroscopy (XPS) measurements were performed with an Ulvac PHI 5000 Versa Probe setup equipped with a monochromatic Al Kα (1486.6 eV) excitation source. The binding energies of each photoelectron line were charge-referenced to the adventitious C 1*s* line at 284.8 eV. The high-resolution XPS data were fitted with the Shirley backgrounds and Lorentzian functions using CasaXPS software.

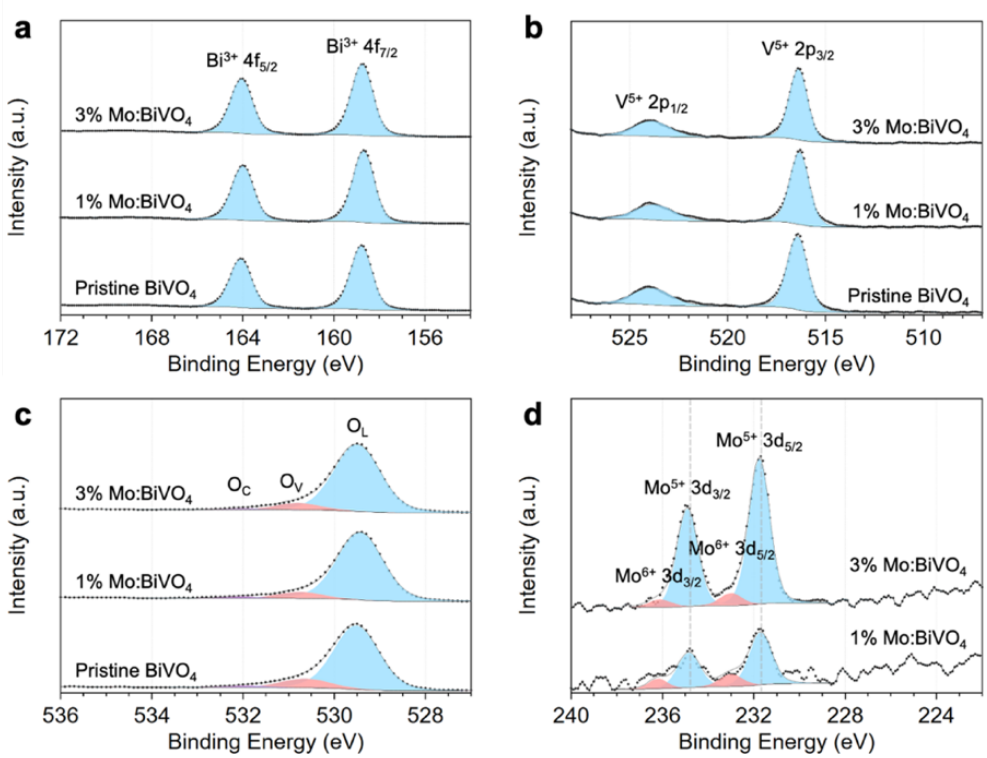

Fig. S4 X-ray photoemission spectra in the (a) Bi 4*f*, (b) V 2*p*, (c) O 1*s*, and (d) Mo 3*d* regions.

Table S2 List of the oxygen vacancy (O_V) to lattice oxygen (O_L) ratios in the O 1*s* XPS and the Mo^{6+}/Mo^{5+} ratios in Mo 3*d* XPS.

Sample	O_V / O_L	Mo^{6+} / Mo^{5+}
Pristine $BiVO_4$	0.16	-
1% Mo:$BiVO_4$	0.10	0.25
3% Mo:$BiVO_4$	0.11	0.09

X-ray absorption spectroscopy (XAS) at the Bi L_3-edge was performed at beamline TLS 01C1 of the National Synchrotron Radiation Research Center (NSRRC), Taiwan, in total fluorescence yield (TFY) mode, while O K-edge and V L-edge XAS were measured at beamline TLS 20A1, NSRRC, in total electron yield (TEY) mode.

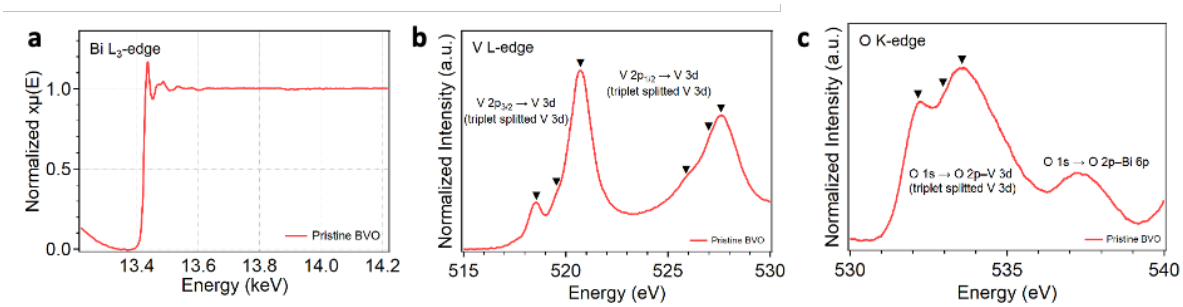

Fig. S5 (a) Bi L_3-edge, (b) V L-edge, and (c) O K-edge X-ray absorption spectra measured from a pristine $BiVO_4$ photoanode.

3. Photoelectrocatalytic Oxidation of Benzyl Alcohol

All (photo)electrochemical measurements were performed in a custom-built, undivided Teflon cell (**Fig. S6**). The three-electrode setup consisted of a 1.00 × 1.25 cm^2 $BiVO_4$ film as the working electrode, a Pt foil as the counter electrode, and an $Ag/AgNO_3$ (0.01 M in CH_3CN) pseudo-reference electrode, all connected to a Metrohm PGSTAT204 potentiostat. The $Ag/AgNO_3$ pseudo-reference electrode was periodically calibrated using cyclic voltammetry in a 2 mM ferrocene (Fc) solution in CH_3CN, with Pt working and counter electrodes. The Fc/Fc^+ half-wave potentials, averaged over varying scan rates (see **Fig. S7** and **Table S3**), allow the applied potentials in this work to be referenced to the Fc/Fc^+ redox couple by:

$$E_{Fc/Fc+} = E_{Ag/AgNO3} - 0.0771\ V$$

The electrolyte solution was 0.1 M $LiClO_4$ (>99%, Thermo Scientific) in 20 mL CH_3CN (>99.9%, Thermo Scientific), and 0.5 mmole benzyl alcohol (>99%, Alfa Aesar), 0.2 mmole *N*-hydroxysuccinimide (NHS; >98%, Thermo Scientific), and 2 mmole pyridine (>99%, Thermo Scientific) were also added as needed. The illumination was provided by an AM 1.5G solar simulator (LSH 7320, Newport) through a quartz window on the Teflon cell onto the FTO side of the $BiVO_4$ films. Constant-potential photoelectrocatalysis was conducted at an applied potential of 0.5 V vs. $Ag/AgNO_3$.

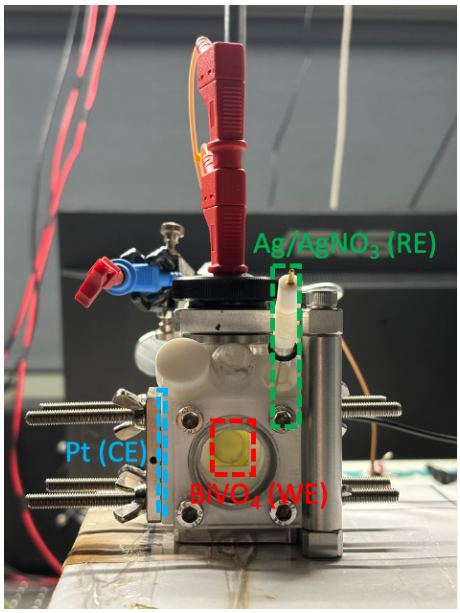

Fig. S6 Photograph of the custom-built Teflon cell used for photoelectrocatalytic benzyl alcohol oxidation.

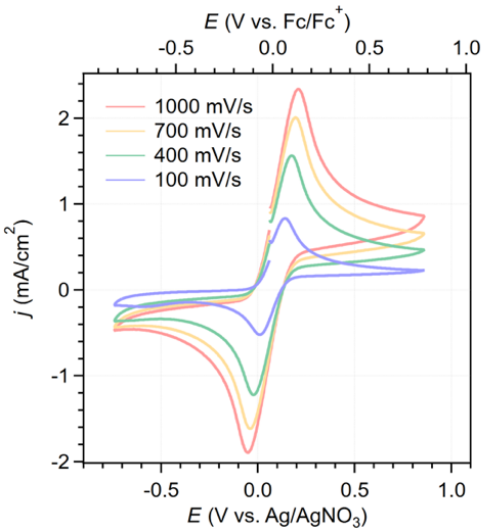

Fig. S7 Cyclic voltammograms of 2 mM Fc in CH_3CN with $Ag/AgNO_3$ reference electrode at different scan rates.

Table S3 Summarized anodic and cathodic peak potentials (E_{pa}, E_{pc}), half-wave potentials ($E_{1/2}$), and peak currents (j_{pa}, j_{pc}) from the Fc voltammograms.

Scan Rate (V s^{-1})	E_{pa} (V)	E_{pc} (V)	ΔE_p (V)	$E_{1/2}$ (V)	j_{pa} (mA)	j_{pc} (mA)	$\lvert j_{pa}/j_{pc} \rvert$
1.0	0.2089	–0.0523	0.2612	0.0783	2.365	–2.249	1.052
0.7	0.1942	–0.0377	0.2319	0.0783	2.033	–1.915	1.062
0.4	0.1747	–0.0230	0.1978	0.0759	1.572	–1.453	1.082
0.1	0.1405	0.0111	0.1294	0.0758	0.8205	–0.6748	1.216

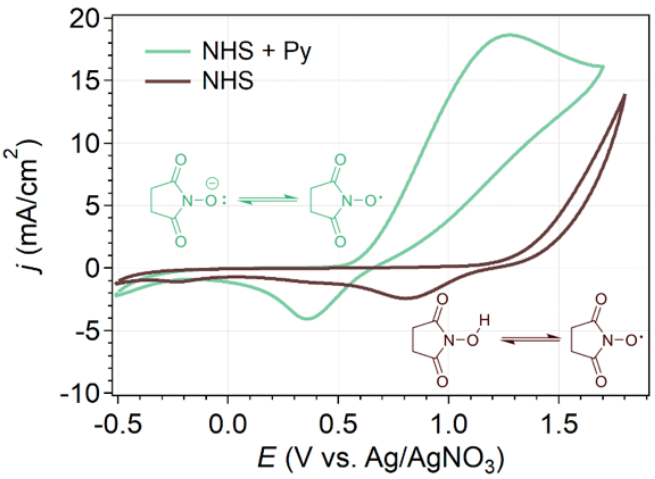

Fig. S8 Cyclic voltammograms of 50 mM NHS in acetonitrile using a Pt working electrode, with (green) and without (brown) 100 mM pyridine, illustrating the cathodic shift in oxidation potential upon NHS deprotonation.

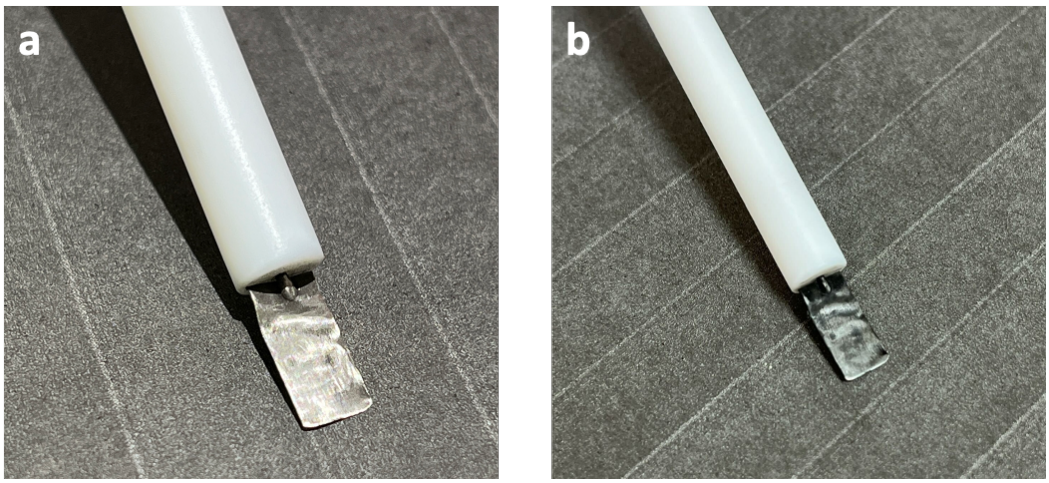

Fig. S9 The Pt foil used as the counter electrode (a) before and (b) after photoelectrocatalytic BnOH oxidation at 0.5 V vs. $Ag/AgNO_3$.

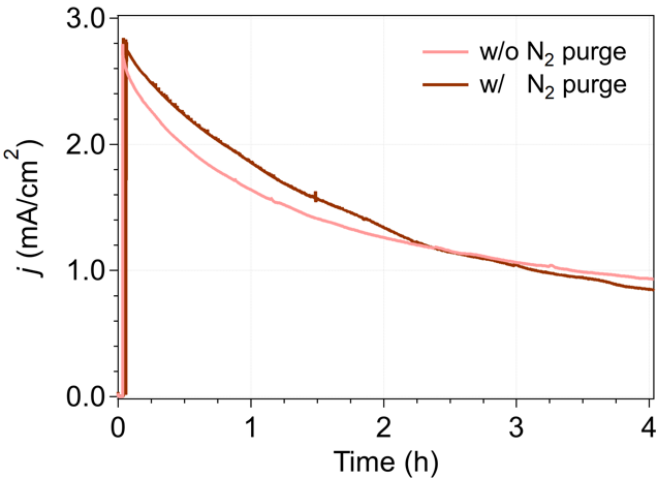

Fig. S10 Comparison of chronoamperometric scans with or without 30 min of N_2 purge prior to NHS-mediated PEC BnOH oxidation with the electrolyte solution in acetonitrile.

To analyze the adsorbed NHS species, the $BiVO_4$ photoanode was rinsed with 5 mL of acetone after 4 h of constant-potential photoelectrocatalysis at 0.5 V vs. $Ag/AgNO_3$. The acetone wash was then evaporated to dryness using a rotary evaporator, and the residue was dissolved in 0.5 mL of DMSO-d_6 for analysis. The resulting solution was subjected to ^1H NMR spectroscopy using a Bruker AVIII HD 400 MHz system. As a control, a pristine $BiVO_4$ sample was immersed in the reaction mixture (acetonitrile, $LiClO_4$, NHS, pyridine, and BnOH) without applying external bias or illumination, and treated identically.

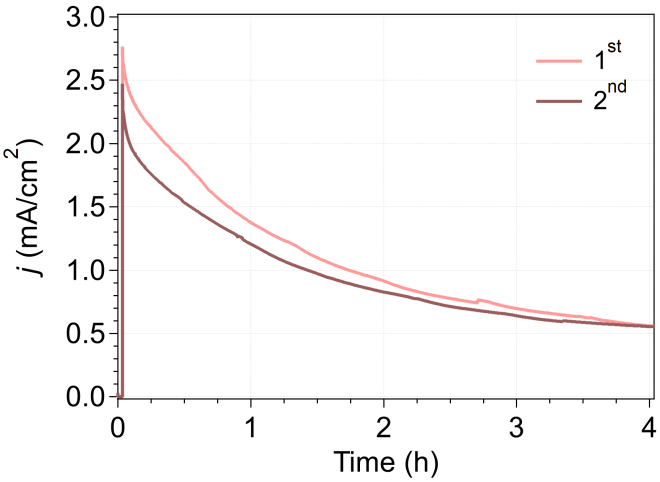

Fig. S11 Two consecutive chronoamperometric scans for NHS-mediated PEC BnOH oxidation using the same pristine $BiVO_4$ photoanode under AM 1.5 G simulated solar illumination. The applied potential was set at 0.5 V vs. $Ag/AgNO_3$.

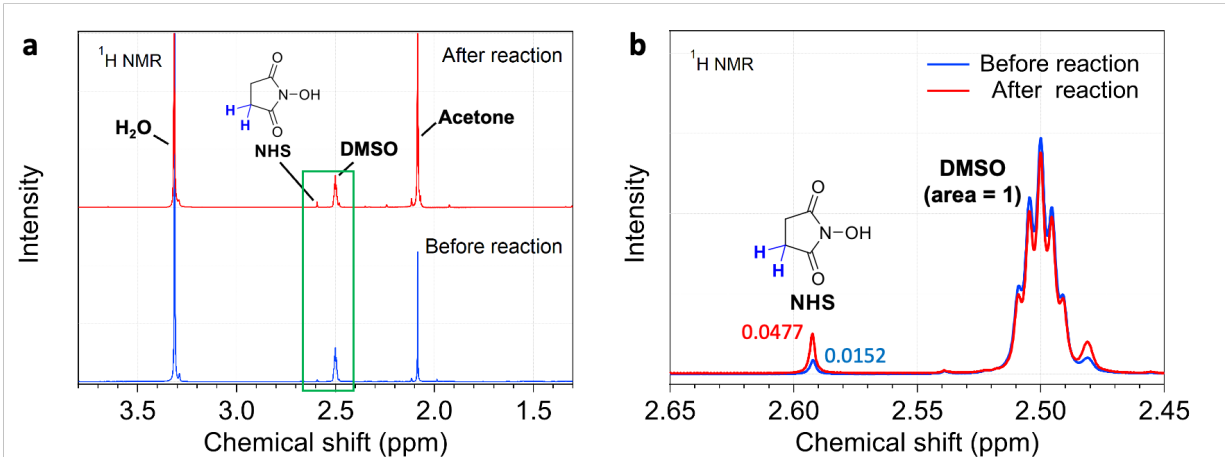

Fig. S12 Comparison of the ^{1}H NMR spectra of the acetone wash solutions used to rinse the $BiVO_4$ photoanode before and after 4 hours of mediated PEC BnOH oxidation at 0.5 V vs. $Ag/AgNO_3$.

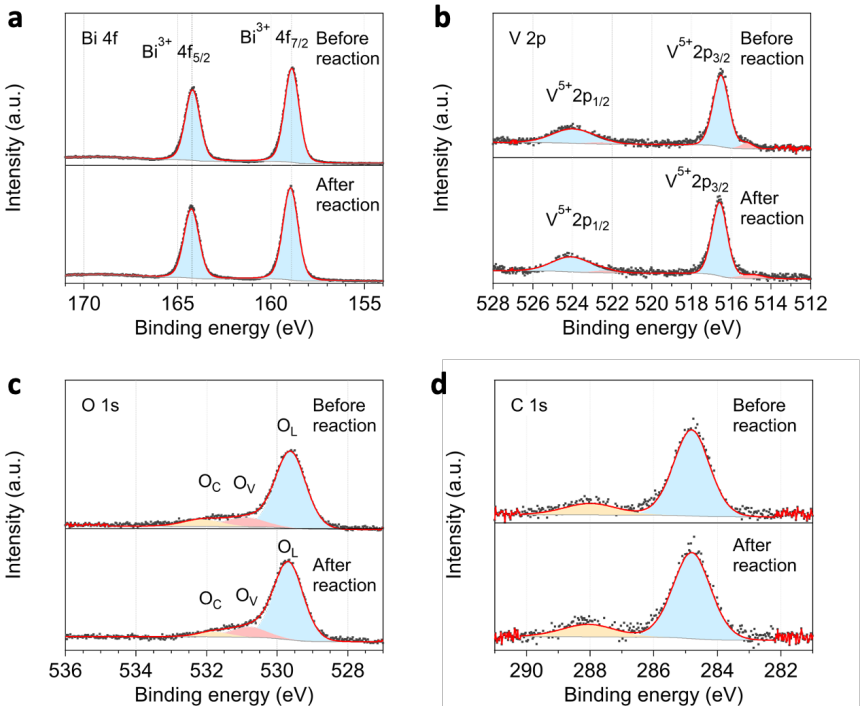

Fig. S13 Comparison of X-ray photoemission (XPS) spectra in the (a) Bi 4*f*, (b) V 2*p*, (c) O 1*s*, and (d) C 1*s* regions for a pristine $BiVO_4$ photoanode before and after 4 h of constant-potential photoelectrocatalytic BnOH oxidation at 0.5 V vs. $Ag/AgNO_3$.

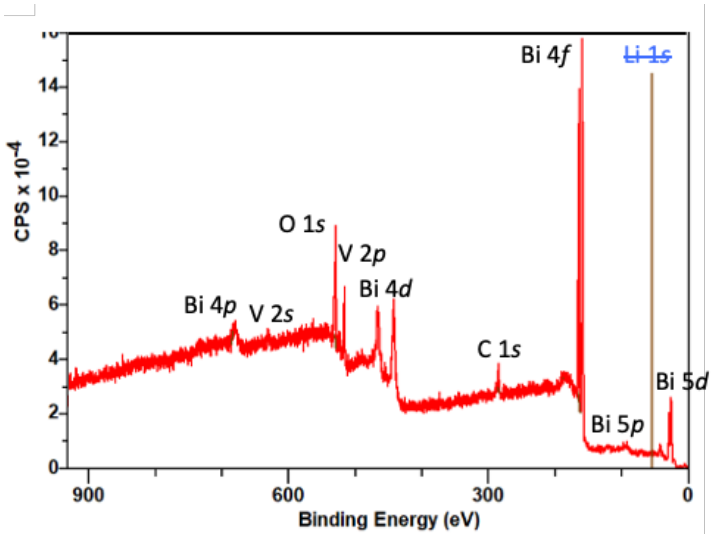

Fig. S14 XPS survey spectrum of a pristine $BiVO_4$ photoanode after 4 h of constant-potential photoelectrocatalytic BnOH oxidation.

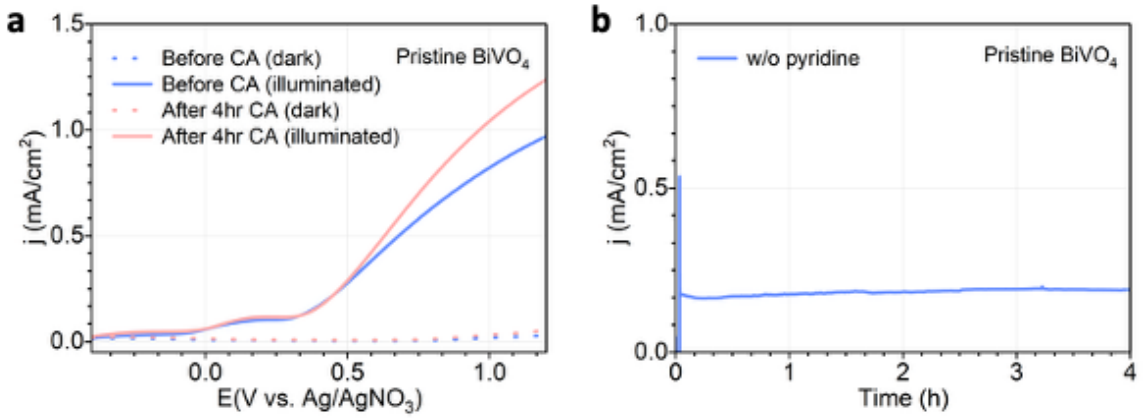

Fig. S15 (a) The LSV curves and (b) chronoamperometric response at 0.5 V vs. $Ag/AgNO_3$ measured from a pristine $BiVO_4$ photoanode when performing NHS-mediated photoelectrocatalytic BnOH oxidation in the absence of pyridine.

Photoelectrochemical impedance spectroscopy (PEIS) was performed using a ZENNIUM PRO potentiostat (Zahner-Elektrik) in the frequency range of 800 mHz to 200 kHz at AC perturbation amplitudes of 20 mV. Measurements were conducted at 0.5 V vs. $Ag/AgNO_3$. All impedance data were analyzed using Zahner Analysis software.

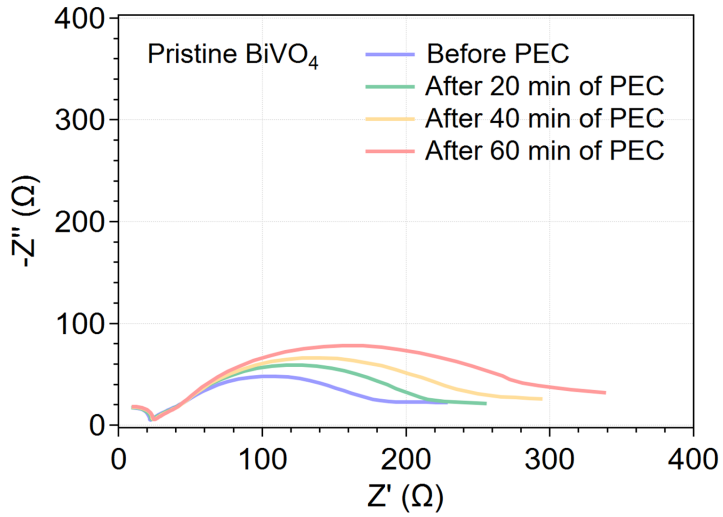

Fig. S16 PEIS Nyquist plots collected at 0.5 V vs. $Ag/AgNO_3$ under illumination, showing progressive growth of the low-frequency semicircle during NHS-mediated photoelectrocatalysis, indicative of increasing interfacial charge transfer resistance due to NHS^- adsorption.

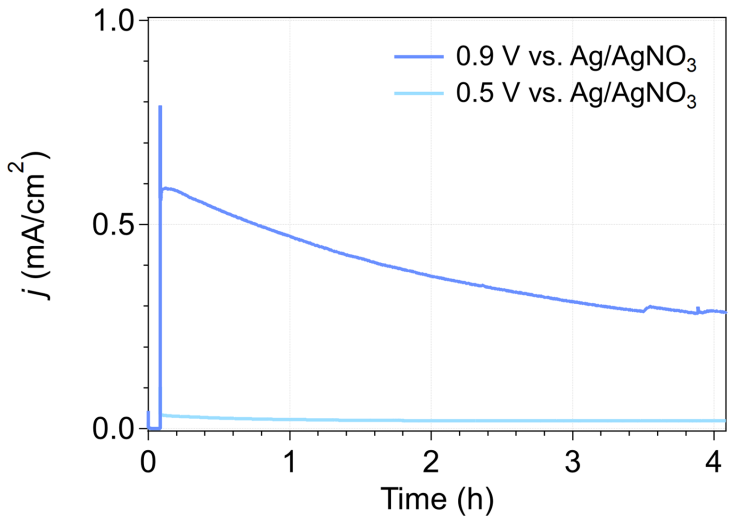

Fig. S17 Chronoamperometric scans of direct photoelectrocatalytic BnOH oxidation at 0.5 V and 0.9 V vs. $Ag/AgNO_3$ without the addition of any redox mediator.

Reaction products were analyzed by a Shimadzu GC-2010 gas chromatography (GC) system equipped with a Trajan™ BP1 fused silica capillary column (60 m × 0.53 mm ID × 3.0 µm) and a flame ionization detector. A 1 µL aliquot of the reaction mixture was injected via autosampler, with N_2 as the carrier gas at a 3.0 mL min^{-1} flow rate. The column temperature was initially set at 60°C for 1 minute, then ramped to 100°C at 10.0°C min^{-1}, and held for 10 minutes. It was then increased to 150°C at 20.0°C min^{-1} and held for 3 minutes, followed by a final ramp to 250°C at 40°C min^{-1}, held for 3 minutes.

The yield rate of BA was calculated by dividing the number of moles of BA produced (n_{BA}), as obtained by GC analysis, by the geometric surface area of the $BiVO_4$ photoanode (A_{geo}) and the reaction time (t):

$$BA\ production\ rate(\mu mol\ cm^{-2}\ h^{-1}) = \frac{n_{BA}(\mu mol)}{A_{geo}(cm^2) \times t(h)}$$

The Faradaic efficiency (FE) of each photoelectrocatalytic reaction was calculated using n_{BA} and the integrated charge (Q) passing through the $BiVO_4$ photoanode:

$$FE(\%) = \frac{n_{BA}(mol) \times 2 \times 96485(C\ mol^{-1})}{Q(C)} \times 100\%$$

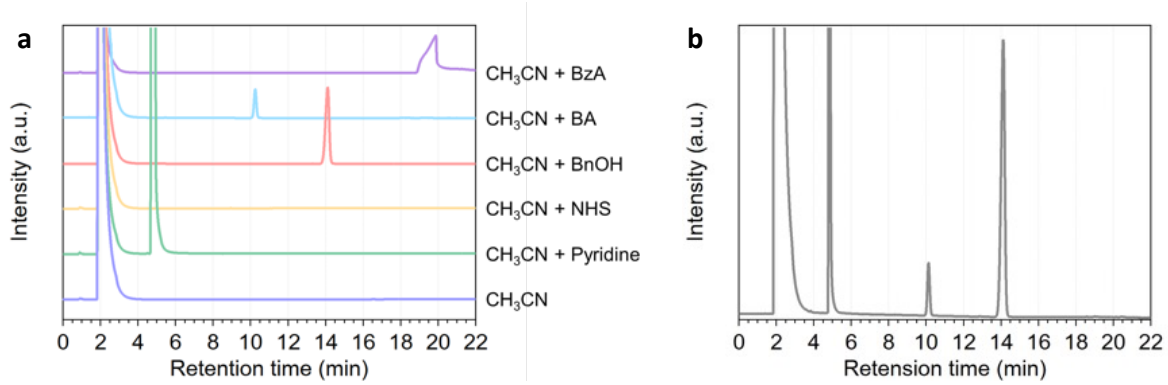

Fig. S18 (a) Reference gas chromatograms of benzyl alcohol (BnOH), benzaldehyde (BA), benzoic acid (BzA), NHS, and pyridine dissolved in CH_3CN. (b) GC analysis result following 4 h of constant-potential photoelectrocatalysis reveals the presence of BA and the absence of BzA in the reaction mixture.

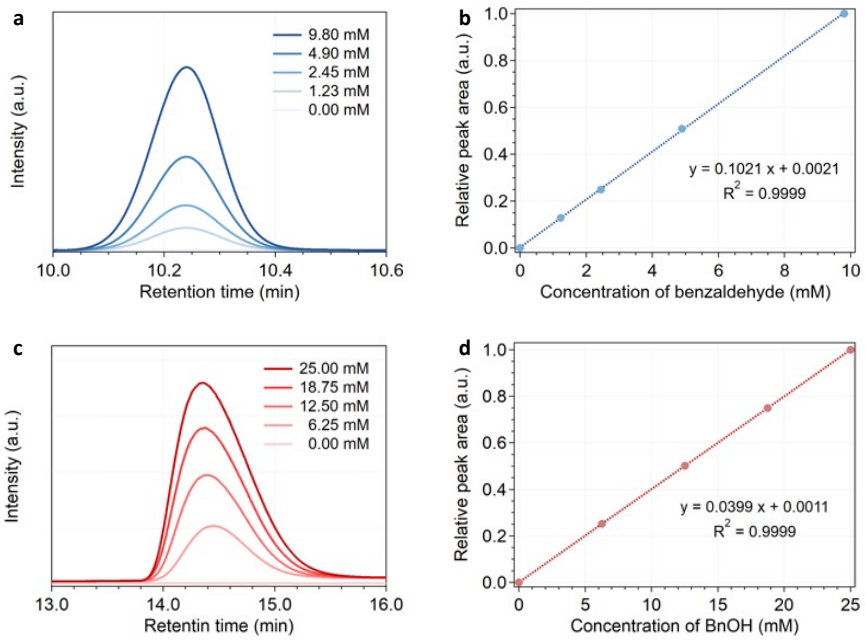

Fig. S19 Enlarged gas chromatograms of standard (a) benaldehyde (BA) and (c) benzyl alcohol (BnOH) solutions in CH_3CN. The integrated BA and BnOH peak areas are used to construct the calibration curves in (b) and (d), respectively.

4. Effects of Different Redox Mediators and Supporting Electrolytes

N-hydroxyphthalimide (NHPI; 98%, Combi-Blocks) and 2,2,6,6-tetramethylpiperidinyl-1-oxyl (TEMPO; 98+%, Thermo Scientific) were used instead of NHS as the redox mediator. In addition to $LiClO_4$, alternative supporting electrolytes used in this study include $LiBF_4$ (98%, Sigma-Aldrich), $NaClO_4$ (99+%, Acros), KPF_6 (99%, Thermo Scientific), $^nBu_4NClO_4$ (99+%, Thermo Scientific), and $^nBu_4NPF_6$ (98%, Thermo Scientific), all with 0.1 M concentration in CH_3CN.

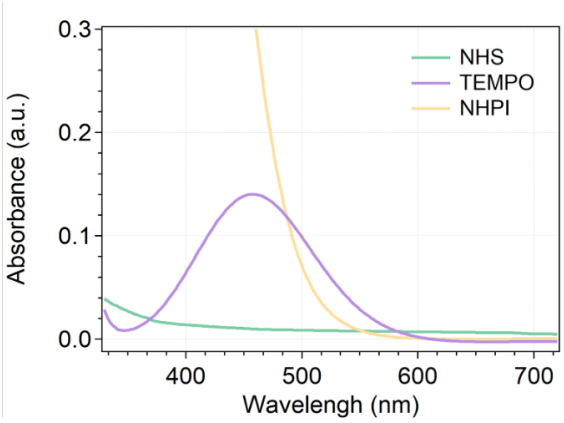

Fig. S20 UV-vis absorption spectra of the reaction mixtures when NHPI and TEMPO were used as the redox mediator instead of NHS.

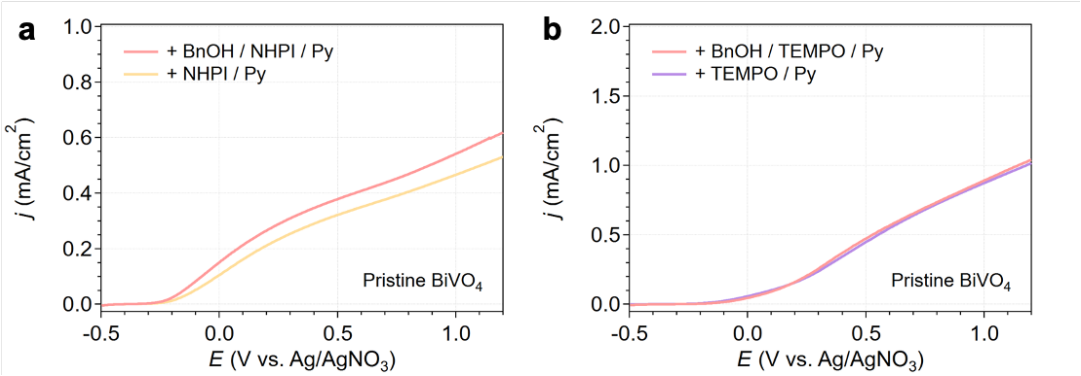

Fig. S21 The LSV curves for (a) NHPI-mediated and (b) TEMPO-mediated photoelectrocatalytic BnOH oxidations.

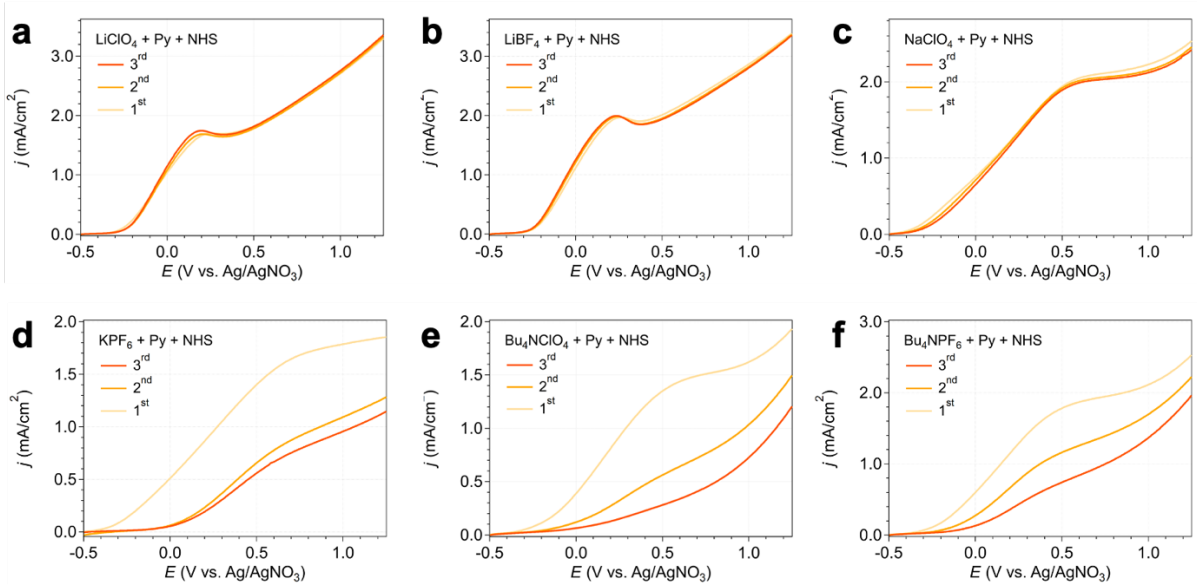

Fig. S22 Comparison of three consecutive LSV scans using a pristine $BiVO_4$ photoanode in 0.1 M (a) $LiClO_4$, (b) $LiBF_4$, (c) $NaClO_4$, (d) KPF_6, (e) $^nBu_4NClO_4$, and (f) $^nBu_4NPF_6$, in addition to 10 mM NHS and 0.1 M pyridine.

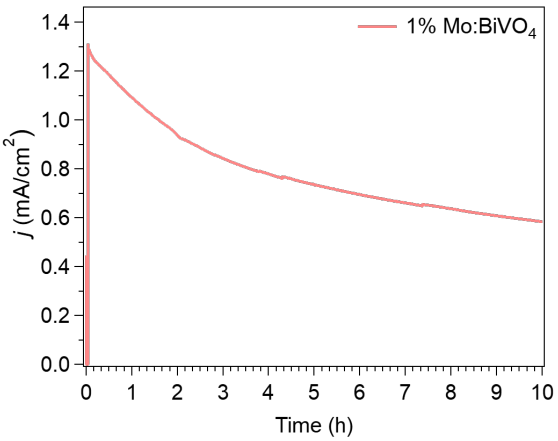

Fig. S23 Chronoamperometric response measured at 0.5 V vs. $Ag/AgNO_3$ for NHS-mediated photoelectrocatalytic BnOH oxidation using 1% Mo-doped $BiVO_4$.

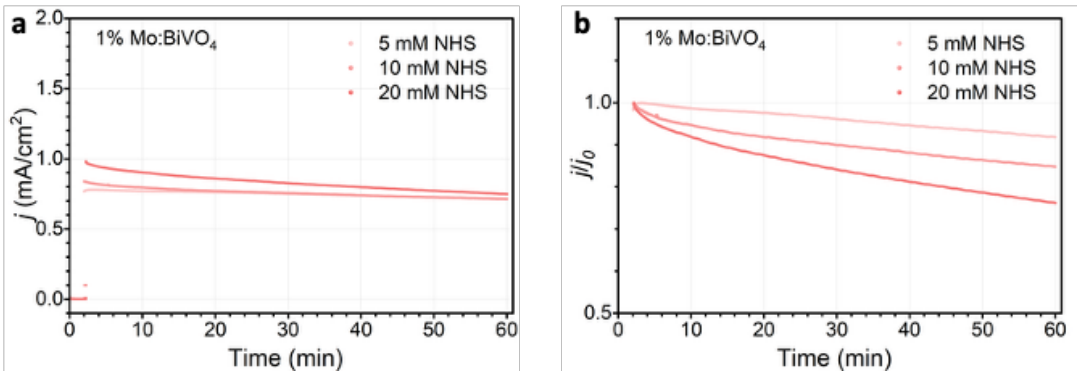

Fig. S24 (a) Chronoamperometric responses measured at 0.5 V vs. $Ag/AgNO_3$ using a 1% Mo-doped $BiVO_4$ photoanode with varying NHS concentrations (5-20 mM), while maintaining constant BnOH (25 mM) and pyridine (100 mM) concentrations. (b) The same curves normalized to the respective initial photocurrent density.

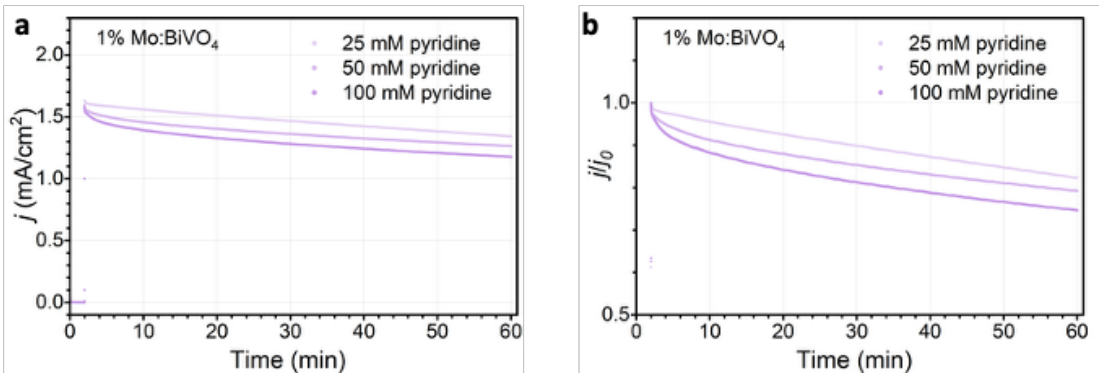

Fig. S25 (a) Chronoamperometric responses measured at 0.5 V vs. $Ag/AgNO_3$ using a 1% Mo-doped $BiVO_4$ photoanode with varying pyridine concentrations (25-100 mM), while maintaining constant BnOH (25 mM) and NHS (10 mM) concentrations. (b) The same curves normalized to the respective initial photocurrent density.

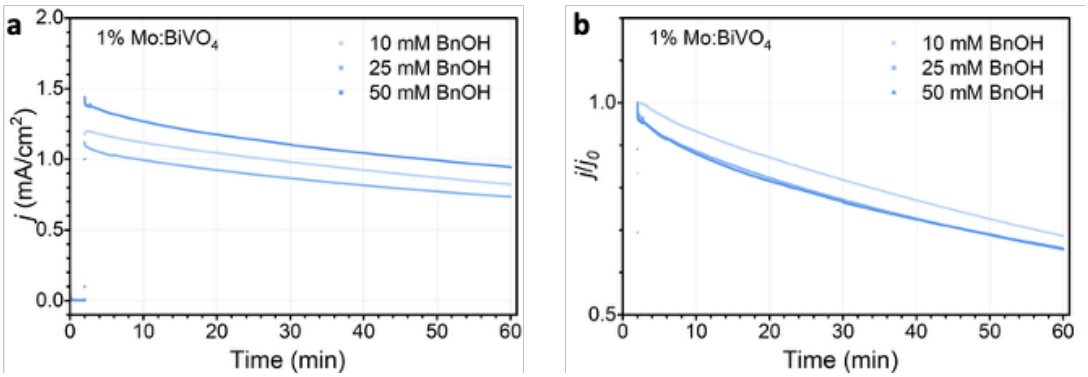

Fig. S26 (a) Chronoamperometric responses measured at 0.5 V vs. $Ag/AgNO_3$ using a 1% Mo-doped $BiVO_4$ photoanode with varying BnOH concentrations (10, 25, and 50 mM), while maintaining constant NHS (10 mM) and pyridine (100 mM) concentrations. (b) The same curves normalized to the respective initial photocurrent density.

5. Comparison of pristine and Mo-doped $BiVO_4$ in photoelectrocatalysis in both aqueous and non-aqueous environments

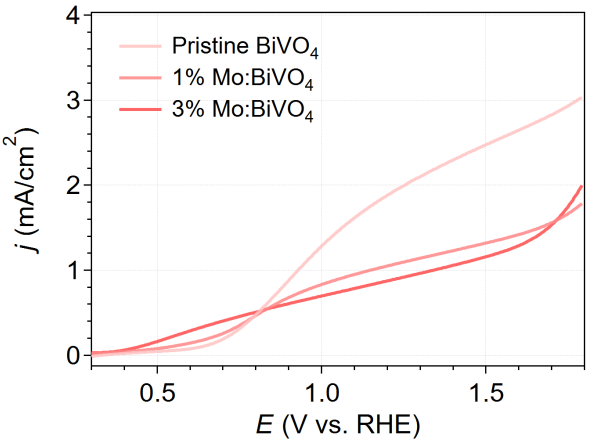

Fig. S27 LSV scans of pristine $BiVO_4$, 1% Mo:$BiVO_4$, and 3% Mo:$BiVO_4$ in 0.1 M Na_2SO_4 (pH = 6.8) with the addition of 0.1 M Na_2SO_3 as sacrificial hole acceptor.

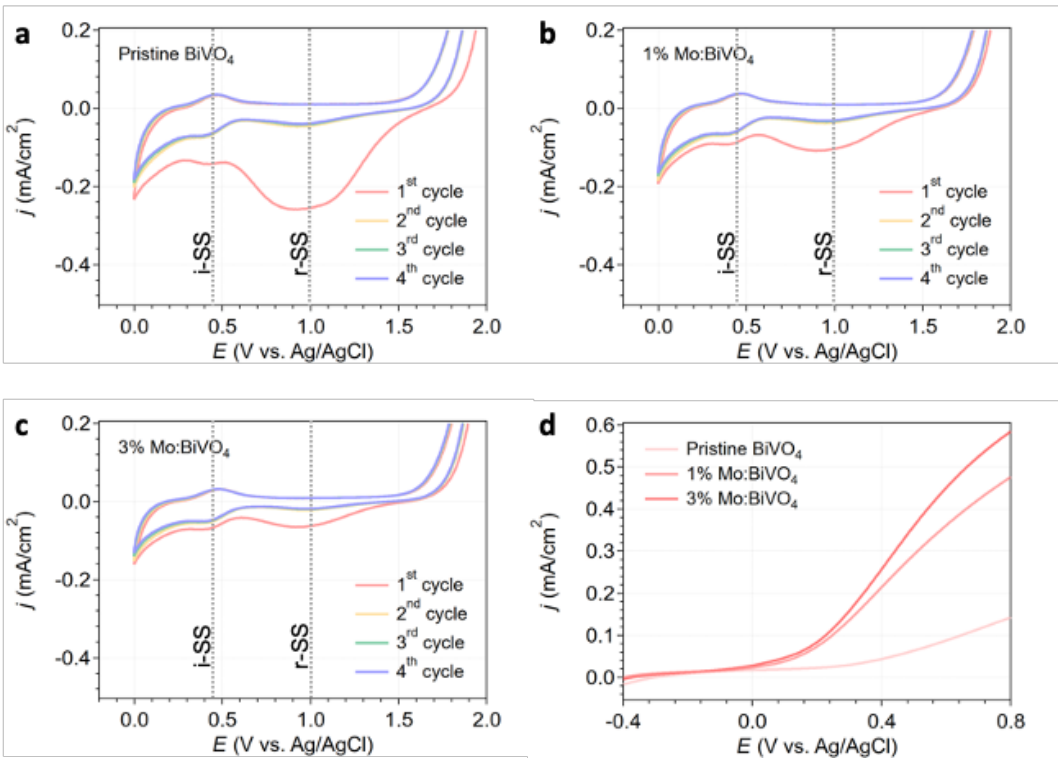

Fig. S28 (a-c) Cyclic voltametric scans of (a) pristine $BiVO_4$, (b) 1% Mo:$BiVO_4$, and (c) 3% Mo:$BiVO_4$ between 2.0 V to 0.0 V vs. Ag/AgCl in 0.1 M Na_2SO_4 (pH = 6.8) using a 2000 mV sec^{-1} scan rate. Features corresponding to the intermediate-type and recombination-type surface states are noted as i-SS and r-SS, respectively. (d) LSV scans of three photoanodes in 0.1 M Na_2SO_4, providing photocurrent for driving OER.

For each of the pristine $BiVO_4$, 1% Mo:$BiVO_4$, and 3% Mo:$BiVO_4$, the PEC BnOH oxidation reaction was performed using four independently prepared photoanodes. The product analysis results and the time constants used to fit the photocurrent density decay at 0.5 V vs. $Ag/AgNO_3$ are tabulated in **Table S4-S6**.

Table S4 BA production rates, Faradaic efficiencies (FE), and photocurrent decay rate constants measured from four pristine $BiVO_4$ photoanodes.

Trial	BA Production Rate (μmol cm^{-2} h^{-1})	FE (%)	τ_{trap} (min)	τ_{ad} (min)
1	9.1	94.9	11.9	64.8
2	7.6	87.6	10.4	96.0
3	11.1	99.9	4.6	95.5
4	7.3	98.9	5.4	74.2
Average	8.8 ± 0.9	95.3 ± 2.8	8.1 ± 1.8	82.6 ± 7.8

Table S5 BA production rates, Faradaic efficiencies (FE), and photocurrent decay rate constants measured from four 1% Mo:$BiVO_4$ photoanodes.

Trial	BA Production Rate (μmol cm^{-2} h^{-1})	FE (%)	τ_{ad} (min)
1	18.0	97.8	161.4
2	15.9	88.2	135.6
3	22.2	87.7	96.4
4	20.5	95.1	134.3
Average	19.1 ± 1.4	92.2 ± 2.5	131.9 ± 13.4

Table S6 BA production rates, Faradaic efficiencies (FE), and photocurrent decay rate constants measured from four 3% Mo:$BiVO_4$ photoanodes.

Trial	BA Production Rate (μmol cm^{-2} h^{-1})	FE (%)	τ_{ad} (min)
1	13.5	98.1	187.5
2	14.4	97.1	129.3
3	16.2	94.9	238.2
4	21.5	89.7	136.6
Average	16.4 ± 1.8	94.9 ± 1.9	172.9 ± 25.3

6. Density Functional Theory (DFT) Computational Method

First-principles calculations were performed using the Vienna Ab initio Simulation Package (VASP).[3] The Perdew–Burke–Ernzerhof (PBE) functional within the Generalized Gradient Approximation (GGA)[4] and the projector augmented-wave (PAW) method[5] were employed to treat exchange-correlation and core-valence interactions, respectively. The valence electron configurations were Bi ($5d^{10}6s^26p^3$), V ($3p^63d^34s^2$), Mo ($4p^64d^55s^1$), and O ($2s^22p^4$). A plane-wave cutoff energy of 500 eV was used for all calculations.

To account for on-site Coulomb interaction, GGA+U correlations were applied with U = 2.7 eV for V and 2.3 eV for Mo, based on the previous studies.[6–9] The Brillouin zone was sampled using Γ-centered Monkhorst–Pack meshes (6×7×3 for bulk; 6×6×1 for surface) with a reciprocal spacing of 0.03 $Å^{-1}$. Structural optimization used Gaussian smearing (0.1 eV) and convergence thresholds of 10^{-5} eV per atom for total energy and 0.02 eV $Å^{-1}$ for atomic forces. Spin polarization was considered in dopant and defect models.

Monoclinic scheelite $BiVO_4$ (space group $I_{2/b}$) was modeled based on the Wycoff positions reported by Lotfi et al. [10] The $BiVO_4$(001) facet was selected as being the most stable stoichiometric surface,[11,12] and its surface energy was calculated as:

$$\gamma = \frac{(E_{slab} - n\,E_{bulk})}{2A}$$

where E_{slab} and E_{bulk} are the total energies of the slab and bulk models, A is the surface area, and γ is the surface energy per unit area (J m^{-2}). A vacuum spacing of 15 Å was added atop the surface. In slab models, only atomic positions were relaxed, with in-plane lattice constants fixed to the bulk-optimized values. The computed surface energy of $BiVO_4$(001) was 0.309 J m^{-2}, consistent with prior reports.[11,12] All dopant and defect calculations were based on a 2×2×1 supercell containing six Bi/V atomic layers (**Fig. S*30***).

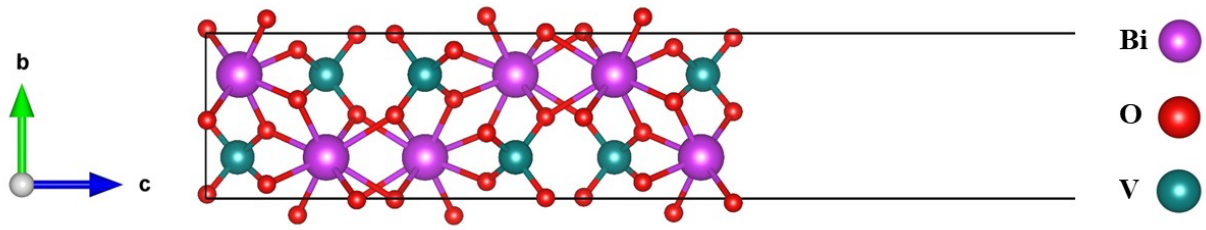

Fig. S29 Optimized oxygen-terminated $BiVO_4$(001) facet.

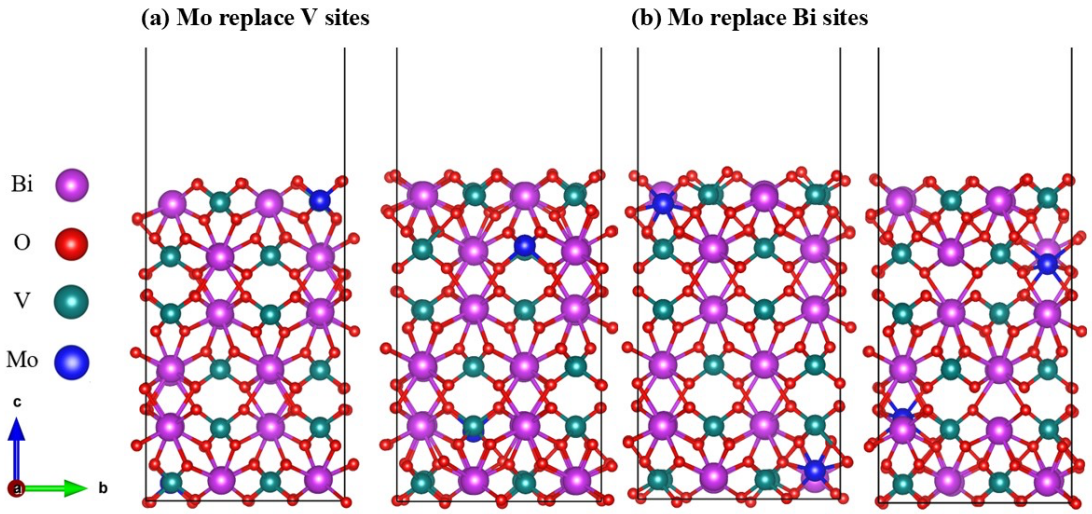

Fig. S30 The optimized structures of Mo-doped $BiVO_4$(001) slabs with Mo substituting the (a) V sites and (b) Bi sites on the topmost layer and the sublayer.

To evaluate Mo doping, we assessed the relative stability of Mo substitution at Bi or V sites, both at the surface and sublayer. Dopant formation energies were calculated as:

$$E_{form} = \frac{\left(E_{doped} - E_{pristine} - 2\mu_{Mo} + 2\mu_{M}\right)}{2}$$

where E_{doped} and $E_{pristine}$ are the total energies of the doped and pristine slabs, and μ_{Mo}, μ_{M} are the chemical potentials of Mo and the replaced metal (M = Bi or V). Values under the O-poor condition were adopted from prior work[13] and summarized in **Table S7**. Mo was found to preferentially substitute topmost V sites (**Table S8**), which was used as the reference doped configuration.

Table S7 Chemical potentials used for each atom in DFT computation.

	μ (O-rich) (eV)	μ (O-poor) (eV)
Bi	–7.98	–4.29
V	–18.00	–11.85
O	–6.16	–8.62
Mo	–18.46	–11.48

Oxygen vacancies were examined at two inequivalent O sites adjacent to either V or Mo in pristine and Mo-doped $BiVO_4$(001) slabs. Vacancies were introduced systematically at the top and bottom surfaces, and formation energies were calculated as:

$$E_{V_O} = \frac{\left(E_{defect} - E_{reference} + 2 \times \mu_{O}\right)}{2}$$

where E_{defect} and $E_{reference}$ are the total energies of defective and pristine (or Mo-doped) surfaces, and μ_O is the chemical potential of oxygen under O-poor condition.

Table S8 Formation energies (in eV) for Mo situated in different metal sites in the $BiVO_4$(001) slab under both oxygen-rich and oxygen-poor conditions.

Mo doped sites	O-rich	O-poor
V (topmost)	–1.021	–1.44
V (sublayer)	–0.363	–0.78
Bi (topmost)	5.614	–1.27
Bi (sublayer)	6.092	–0.79

Reference

(1) Tu, G.-Z.; Chen, J.-Y.; Zhen, Z.-X.; Li, Y.; Chang, C.-W.; Chang, W.-J.; Chen, H. M.; Jiang, C.-M. Elucidating the Epitaxial Growth Mechanisms of Solution-Derived $BiVO_4$ Thin Films Utilizing Rapid Thermal Annealing. *ACS Appl. Electron. Mater.* **2024**, *6* (3), 1872–1885.

(2) Cooper, J. K.; Gul, S.; Toma, F. M.; Chen, L.; Liu, Y.-S.; Guo, J.; Ager, J. W.; Yano, J.; Sharp, I. D. Indirect Bandgap and Optical Properties of Monoclinic Bismuth Vanadate. *J. Phys. Chem. C* **2015**, *119* (6), 2969–2974.

(3) Kresse, G.; Furthmüller, J. Efficient Iterative Schemes for *Ab Initio* Total-Energy Calculations Using a Plane-Wave Basis Set. *Phys. Rev. B* **1996**, *54* (16), 11169–11186.

(4) Perdew, J. P.; Burke, K.; Ernzerhof, M. Generalized Gradient Approximation Made Simple. *Phys. Rev. Lett.* **1996**, *77* (18), 3865–3868.

(5) Blöchl, P. E. Projector Augmented-Wave Method. *Phys. Rev. B* **1994**, *50* (24), 17953–17979.

(6) Park, H. S.; Kweon, K. E.; Ye, H.; Paek, E.; Hwang, G. S.; Bard, A. J. Factors in the Metal Doping of $BiVO_4$ for Improved Photoelectrocatalytic Activity as Studied by Scanning Electrochemical Microscopy and First-Principles Density-Functional Calculation. *J. Phys. Chem. C* **2011**, *115* (36), 17870–17879.

(7) Cen, J.; Li, S.; Zheng, J.; Pan, F. Electron Polarons in the Subsurface Layer of Mo/W-Doped $BiVO_4$ Surfaces. *RSC Adv.* **2019**, *9* (2), 819–823.

(8) Wang, W.; Strohbeen, P. J.; Lee, D.; Zhou, C.; Kawasaki, J. K.; Choi, K. S.; Liu, M.; Galli, G. The Role of Surface Oxygen Vacancies in $BiVO_4$. *Chem. Mater.* **2020**, *32* (7), 2899–2909.

(9) Zhang, Z.; Song, Y.; Xiang, Y.; Zhu, Z. Vacancy Defect Engineered BiVO4 with Low-Index Surfaces for Photocatalytic Application: A First Principles Study. *RSC Adv.* **2022**, *12* (48), 31317–31325.

(10) Lotfi, S.; Assani, A.; Saadi, M.; Ait Ahsaine, H. Synthesis, Structural and Microstructural Properties of Bismuth Vanadate $BiVO_4$. *Mater Today Proc* **2023**.

(11) Shi, J.; Zhang, W.; Gu, Q. Ab Initio Calculation of Surface-Controlled Photocatalysis in Multiple-Phase $BiVO_4$. *J. Phys. Chem. C* **2022**, *126* (22), 9541–9550.

(12) Li, G. L. First-Principles Investigation of the Surface Properties of Fergusonite-Type Monoclinic $BiVO_4$ Photocatalyst. *RSC Adv.* **2017**, *7* (15), 9130–9140.

(13) Chen, X.; Wu, Y.; Deng, M. Sen; Shen, H.; Ding, J.; Wang, W. Effects of Fluorination and Molybdenum Codoping on Monoclinic $BiVO_4$ Photocatalyst by HSE Calculations. *ACS Omega* **2022**, *7* (20), 17075–17082.